

# Preparation of Al–O-Linked Porous-g-C<sub>3</sub>N<sub>4</sub>/TiO<sub>2</sub>-Nanotube Z-Scheme Composites for Efficient Photocatalytic CO<sub>2</sub> Conversion and 2,4-Dichlorophenol Decomposition and Mechanism

Jing Wu,<sup>†</sup> Yujie Feng,<sup>†</sup> B.E. Logan,<sup>‡</sup> Changchao Dai,<sup>†</sup> Xiaoyu Han,<sup>†</sup> Da Li,<sup>\*,†</sup> and Jia Liu<sup>\*,†</sup>

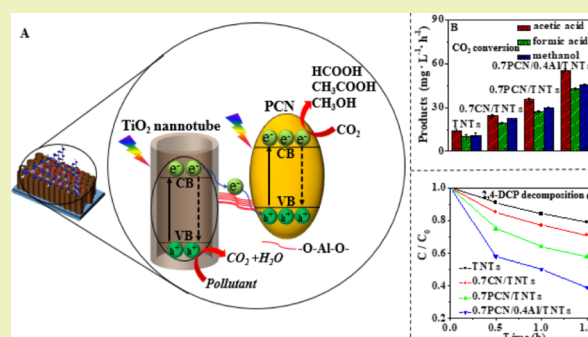
<sup>†</sup>State Key Laboratory of Urban Water Resource and Environment, Harbin Institute of Technology, No 73 Huanghe Road, Nangang District, Harbin 150090, China

<sup>‡</sup>Department of Civil and Environmental Engineering, Penn State University, 212 Sackett Building, University Park, Pennsylvania 16802, United States

## Supporting Information

**ABSTRACT:** The photocatalytic activity of TiO<sub>2</sub> nanotubes can be improved through the construction of a Z-scheme composite, where photogenerated electrons from TiO<sub>2</sub> recombine with the photogenerated holes in a coupled semiconductor. This arrangement allows for improved oxidation due to the residual holes of TiO<sub>2</sub> and better chemical reduction due to the greater availability of the photogenerated electrons of the coupled semiconductor. Efficient Z-scheme porous-g-C<sub>3</sub>N<sub>4</sub>/TiO<sub>2</sub>-nanotube (PCN/TNTs) composites were developed here using a solid sublimation and transition approach, with Al–O links added by an impregnation method to increase interfacial linkages between the PCN and TNTs. The best results for photocatalytic CO<sub>2</sub> conversion were obtained using 0.7PCN/0.4Al/TNTs, as shown by production of  $54.9 \pm 0.70 \text{ mg L}^{-1} \text{ h}^{-1}$  of acetic acid,  $42.7 \pm 0.54 \text{ mg L}^{-1} \text{ h}^{-1}$  of formic acid, and  $45.4 \pm 0.55 \text{ mg L}^{-1} \text{ h}^{-1}$  of methanol, which were about 3.8, 4.3, and 4.2 times that produced with bare TNTs. Photocatalytic 2,4-dichlorophenol decomposition with 0.7PCN/0.4Al/TNTs showed a 40% enhancement compared to bare TNTs in 1.5 h. This Z-scheme composite photocatalyst therefore provides an improved method for more efficient CO<sub>2</sub> conversion or pollutant degradation based on the improved charge separation and linkage of the PCN/TNTs using Al–O.

**KEYWORDS:** Z-scheme, porous-g-C<sub>3</sub>N<sub>4</sub>/TiO<sub>2</sub>-nanotube composites, Al–O links, CO<sub>2</sub> conversion, 2,4-dichlorophenol decomposition



## INTRODUCTION

Efficient conversion of CO<sub>2</sub> to high-value chemicals is a useful strategy for dealing with both environmental problems related to CO<sub>2</sub> emissions and sustainable chemical production.<sup>1–3</sup> Photocatalysis is considered to be one potentially efficient method to reduce CO<sub>2</sub>, and TiO<sub>2</sub> is regarded as one of the best semiconductor photocatalysts owing to its high chemical stability, thermal stability, and low toxicity.<sup>4–6</sup> TiO<sub>2</sub> nanotubes (TNTs) with three-dimensional nanostructures are particularly of interest for CO<sub>2</sub> conversion due to their large surface area, high abundance of active sites, and fast charge transport capacity.<sup>7–10</sup> Moreover, photocatalysis processes can also be used for pollutant degradation. Thus, improved photocatalytic processes have two possible advantages of providing sustainable methods for chemical production using waste CO<sub>2</sub> sources or chemical pollutant degradation. Despite these advantages, the use of TNTs in photocatalytic processes have so far not achieved practical applications,<sup>11</sup> in part due to their wide band gap and low charge separation. Multiple approaches have been utilized to remedy these weaknesses of the TNTs such as building heterojunction composites with another

semiconductor,<sup>12–14</sup> noble-metal deposition,<sup>15,16</sup> and modification with carbon materials.<sup>17,18</sup>

Building heterostructures of TNTs with another semiconductor having a suitable band gap has been shown to increase their photocatalytic activity.<sup>19–21</sup> Two possible mechanisms for the enhanced photogenerated charge separation and transfer in this type of heterostructure system have been considered. One mechanism is the band-to-band transfer, where the photogenerated electrons transfer from the semiconductor with a higher conduction band to another semiconductor with a relatively lower conduction band, whereas the photogenerated holes transfer from the semiconductor with a lower valence band to another semiconductor with a higher valence band. This process creates improved photogenerated charge separation, but the redox capacities of the formed heterostructure composites are reduced in comparison to the individual photocatalysts.<sup>22,23</sup>

Received: May 6, 2019

Revised: July 10, 2019

Published: August 19, 2019

Another charge-transfer mechanism is called the Z-scheme principle. For this transfer mechanism, the photogenerated electrons from  $\text{TiO}_2$  would recombine with the photogenerated holes in the valence band of the coupled semiconductor, allowing the residual photogenerated holes in the valence band of  $\text{TiO}_2$  to have strong oxidizing properties. The residual photogenerated electrons in the conduction band of the coupled semiconductor would then have a strong reducing activity, and therefore improved performance in redox reactions.<sup>24,25</sup> Thus, achieving Z-scheme  $\text{TiO}_2$ -based composites would achieve higher photocatalytic activities than the individual materials.

Graphitic carbon nitride ( $\text{g-C}_3\text{N}_4$ ) has been considered to be a useful material for building Z-scheme composites with  $\text{TiO}_2$  due to suitable conduction and valence band positions, low toxicity, and low cost.<sup>24,26</sup> However, bulk  $\text{g-C}_3\text{N}_4$  has shown poor performance due to its low charge separation and small surface area. The use of  $\text{g-C}_3\text{N}_4$  within the porous structure could enhance visible light absorption and accelerate charge separation and transfer, improving its photocatalytic activity.<sup>27–30</sup> Thus, building porous- $\text{g-C}_3\text{N}_4/\text{TiO}_2$ -nanotube (PCN/TNT) Z-scheme composites should improve photocatalytic performance relative to the individual components.

The lattice mismatching of different constituents in Z-scheme composites can adversely impact the transfer of charge carriers, and therefore more efficient links at the interface of the two semiconductors are needed to improve performance.<sup>31,32</sup> Adding Al–OH functional groups could help to provide links in the  $\text{g-C}_3\text{N}_4/\alpha\text{-Fe}_2\text{O}_3$  heterostructure by replacing the surface hydroxyl groups, resulting in elevated charge transfer and separation.<sup>25</sup> Hence, building Al–O links between PCN and TNTs to make the interface connection tight should improve charge transfer and photocatalytic performance. However, there have been no studies that have examined Al–O-linked PCN/TNTs to create more efficient Z-scheme composites and probe the charge-transfer mechanism of this material.

Al–O-linked PCN/TNTs Z-scheme composites were examined here as a more efficient method for improving both chemical reduction and oxidation. The change in performance was tested by examining  $\text{CO}_2$  reduction to different small molecular weight organic compounds and improved oxidation by photodegradation of 2,4-dichlorophenol (2,4-DCP) as a model organic pollutant. The photogenerated charge separation of the prepared materials was examined using steady-state surface photovoltage spectra, transient-state surface photovoltage (TS-SPV), and concentration of the formed  $\bullet\text{OH}$ . The analysis of this improved Z-scheme composites offers a feasible strategy for designing of TNT-based photocatalysts for different applications related to environmental and energy issues associated with chemical production and pollutant degradation.

## ■ EXPERIMENTAL SECTION

**Reagents.** Ammonium fluoride ( $\text{NH}_4\text{F}$ ), glycerol ( $\text{C}_3\text{H}_8\text{O}_3$ ), aluminium trichloride ( $\text{AlCl}_3$ ), urea ( $\text{CH}_4\text{N}_2\text{O}$ ), sodium bicarbonate ( $\text{NaHCO}_3$ ), and sodium sulfate ( $\text{Na}_2\text{SO}_4$ ) were purchased from Sinopharm Chemical Reagent Co. Ltd. All reagents were of analytical grade and used as received without further purification. Deionized water was used throughout this study.

**Preparation of TNTs.** TNTs were fabricated using an anodization method. Before the anodizing process, Ti foils were soaked in  $\text{H}_2\text{C}_2\text{O}_4$ -bath for 2 h at 98 °C to remove residual oils, rinsed with deionized water, and dried at ambient temperature (20 °C). The

anodized process was performed using a two-electrode setup at a constant voltage of 20 V supplied by a dc power source (MS30SD:0-30V/0-5A) for 2 h at ambient temperature. The electrolyte was a mixture solution of  $\text{NH}_4\text{F}$  (0.5 wt %) and glycerol (60 vol %) in deionized water. The pretreated Ti foil with a radius of 1 cm functioned as the anode, with Pt foil as the cathode. After anodization, this amorphous  $\text{TiO}_2$  was dried at 70 °C for 4 h and annealed at 500 °C for 2 h, to produce the TNTs.

**Preparation of PCN/TNT Composites.** Before preparing PCN/TNT composites, the precursor of PCN was prepared by adding 5 g of urea and 10 g of  $\text{NaHCO}_3$  into a 200 mL beaker with 100 mL of deionized water. The solution in the beaker was stirred using a magnetic stirrer for 4 h, and then the beaker was placed in a refrigerator for freezing. Finally, the beaker was put into a freeze dryer for drying. After freeze drying for 12 h, the precursor of PCN was obtained.

The PCN/TNT composites were produced using a solid sublimation and transition approach. Different amounts of the precursor of porous  $\text{g-C}_3\text{N}_4$  (0.3, 0.5, 0.7 or 0.9 g) were put into a 200 mL crucible, and the TNTs were hung on the crucible 1 cm above the precursors by bending the grip. The crucible was heated in a muffle furnace at 550 °C for 2 h (5 °C/min). The PCN/TNT composites produced using this method were designated as XPCN/TNTs, where X indicates the mass of the PCN precursor. To compare with PCN/TNT composites,  $\text{g-C}_3\text{N}_4/\text{TNT}$  composites were also constructed using a solid sublimation and transition approach by adding 0.7 g of urea into a 200 mL crucible. The procedure was the same as that for fabrication of PCN/TNT composites. The obtained  $\text{g-C}_3\text{N}_4/\text{TNT}$  composites were denoted as 0.7CN/TNTs, where 0.7 indicated the used mass of the urea precursor, and CN indicated  $\text{g-C}_3\text{N}_4$ . In addition, to confirm the Z-scheme mechanism of the photogenerated charge carriers transfer on the prepared composite in the photocatalytic process, PCN (PCN/Ti) sample was fabricated via the same method as that for fabrication of PCN/TNT composites except that TNTs were replaced by pure Ti substrate.

**Preparation of Al–O Linked PCN/TNT Composites.** To obtain the Al–O-linked PCN/TNT composites, Al–O-modified TNTs were first fabricated using an  $\text{AlCl}_3$  aqueous solution (ethanol/water system). The TNTs prepared as described above were immersed in  $\text{AlCl}_3$  solutions (ethanol/water system) with different concentrations (0.1, 0.2, 0.4, or 0.6 M) for 0.5 h. Then, the TNTs were dried at 80 °C for 1 h and calcined at 400 °C for 0.5 h.

Al–O-linked PCN/TNT composites were obtained using the same method as the fabrication of PCN/TNT composites except that the mass of the PCN precursor was constant (0.7 g) and TNTs were replaced with Al–O-modified TNTs. The obtained Al–O-linked PCN/TNT composites were denoted as XPCN/YAl/TNTs, where X indicated the mass of the PCN precursor used, Al indicated that Al–O links were added, and Y indicated the concentration of used  $\text{AlCl}_3$  aqueous solution.

**Characterization of Materials.** X-ray diffraction (XRD) patterns were examined to investigate the crystal phase and composition using a diffractometer (Rigaku D/MAX III-3B) with Cu K radiation, at an applied current of 30 mA with an accelerating voltage of 40 kV. Ultraviolet–vis diffuse reflectance spectra of the samples were measured to investigate the light absorption ability by a spectrophotometer (Shimadzu UV-2550), with  $\text{BaSO}_4$  as the reference. X-ray photoelectron spectroscopy (XPS) was conducted to study the surface element composition using a PHI-5700 ESCA, with an Al K X-ray source and the C 1s peak located at the binding energy of 284.6 eV as a reference to calibrate the binding energies of other elements. Surface morphologies were observed using a field-emission scanning electron microscopy (SEM, FEI Quanta 200F). Transmission electron microscopy (TEM) was conducted with a JEM-3010 electron microscope (JEOL, Japan); the acceleration voltage was 300 kV. Surface photovoltage spectroscopy (SPS) was used to assess the photogenerated charge separation of the samples using a self-assembled system. The monochromatic light source was obtained by passing light from a 500 W xenon lamp (CHFXQ) through a double-prism monochromator (Hilger and Watts, D 300), and a lock-

in amplifier (SR830) together with a light chopper (SR540) to magnify the photovoltage signal. The TS-SPV signal was collected with a self-assembled device. The excited source was derived from a second harmonic Nd: YAG laser (Lab-130-10H, Newport, Co.), the radiation pulse was 355 nm and width was 10 ns. After being amplified by a preamplifier, the signal was recorded by an oscilloscope (Tektronix, DPO 4104B).

**Photoelectrochemical Performance.** Linear sweep voltammetry, transient photocurrent, open-circuit potentials, and electrochemical impedance spectroscopy (EIS) were measured using a three-electrode system with a potentiostat (Princeton Applied Research, Versa STAT3). Pure or modified TNTs were used as the working electrode, Pt foil (99.9%) was used as the counter electrode, and a saturated calomel electrode (SCE, +0.242 V vs standard hydrogen electrode) was used as the reference electrode. The supporting electrolyte was  $\text{Na}_2\text{SO}_4$  (0.1 M). Nitrogen gas (99.999%) was bubbled into the electrolyte throughout the experiment to remove dissolved oxygen from the electrolyte. The frequency in EIS tests was varied from 0.01 to 100 000 Hz, with an amplitude of 10 mV. The detailed data of the electrochemical impedance spectra on the resistance were fitted with the equivalent circuit model of  $R_s(C_{dl}(R_{ct}W))$ , where  $R_s$  means the electrolyte resistance between two electrodes and double-layer capacitance ( $C_{dl}$ ),  $R_{ct}$  means the charge-transfer resistance, and  $W$  means the Warburg impedance.<sup>33</sup> The illumination source was a 150 W xenon lamp (GY-10A, Tuopu Co. Ltd., China), and the light intensity was adjusted to  $100 \text{ mW cm}^{-2}$ . To calculate the incident monochromatic photon to current conversion efficiency (IPCE), the photocurrent densities were tested with different single wavelength irradiation. The IPCE was calculated as

$$\text{IPCE}(\%) = \frac{(1.24 \times 10^3) i}{(\text{wavelength})(I)} \quad (1)$$

where  $i$  ( $\mu\text{A cm}^{-2}$ ) is the photocurrent density, and  $I$  ( $\text{W m}^{-2}$ ) is the measured light intensity. Single wavelength (nm) light was obtained by passing the light of a 500 W xenon lamp (CHFXQ) through a double-prism monochromator (Hilger and Watts, D 300).

**Hydroxyl Radical Test.** The concentration of  $\bullet\text{OH}$  was measured using a fluorescence spectrometer (Jasco. Co. FP-6500). Samples were immersed in terephthalic acid solution ( $5 \times 10^{-4} \text{ M}$ ) in a glass beaker, stirred for 0.5 h, and irradiated for 1 h. Then, a 10 mL sample was withdrawn for measurement with excitation at 315 nm and detection at 425 nm.

**Photocatalytic  $\text{CO}_2$  Conversion and 2,4-DCP Decomposition.** Photocatalytic  $\text{CO}_2$  conversion was examined in a glass reactor with a quartz window to allow transmission of light. Modified TNTs were immersed in  $\text{Na}_2\text{SO}_4$  solution (0.1 M, 60 mL) and irradiated using a 150 W xenon lamp (GY-10A, Tuopu Co. Ltd., China). Prior to irradiation, the  $\text{Na}_2\text{SO}_4$  solution was sparged with pure  $\text{CO}_2$  gas until saturated. After irradiation for 1 h, 1 mL of liquid was withdrawn for analysis of chemical products using a gas chromatograph (Agilent GC 7890A, USA) and an ion chromatograph (IC 6100, Wanyi, Anhui, China).

2,4-DCP decomposition was examined in the same reactor as  $\text{CO}_2$  conversion test using a  $10 \text{ mg L}^{-1}$  solution. Samples were immersed in the 2,4-DCP solution and stirred for 0.5 h in the dark, and then irradiated for 1 h. A 5 mL sample was withdrawn and measured for the chemical concentration using a spectrophotometer (UV-2550, Shimadzu) at an absorption peak of 285 nm.

## RESULTS AND DISCUSSION

**Structural Characterization and Surface Composition.** SEM and TEM were performed to investigate the morphologies of the prepared samples (Figure 1). Pure TNTs showed tubular structures, with an inner diameter of 100 nm, wall thickness of 20 nm, and length of  $1 \mu\text{m}$  (Figure 1A,B). A comparison of the SEM images of 0.7CN/TNTs (Figure 1C) and 0.7PCN/0.4Al/TNTs (Figure 1D) showed that the g-

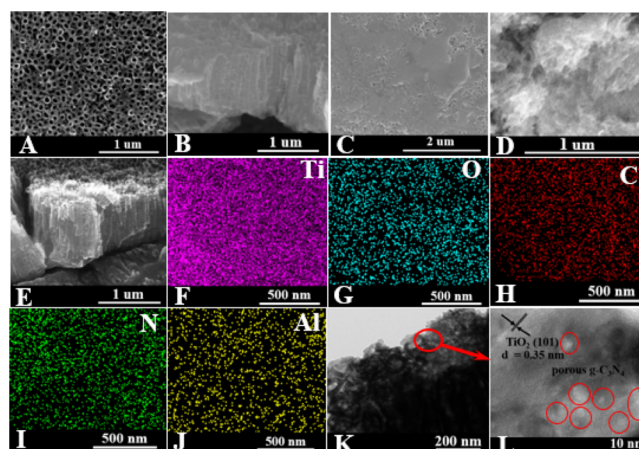


**Figure 1.** SEM images of (A) top and (B) cross-sectional views for bare TNTs. (C) Top view of 0.7CN/TNTs. SEM images of (D) top and (E) cross-sectional views for 0.7PCN/0.4Al/TNTs. (F–J) Element mapping of 0.7PCN/0.4Al/TNTs. (K) TEM and (L) HRTEM images of 0.7PCN/0.4Al/TNTs. The number 0.7 in 0.7CN/TNTs and 0.7PCN/0.4Al/TNTs indicates the mass of  $\text{g-C}_3\text{N}_4$  and PCN precursor, and 0.4 in 0.7PCN/0.4Al/TNTs indicates the concentration of the  $\text{AlCl}_3$  aqueous solution used.

$\text{C}_3\text{N}_4$  on the 0.7PCN/0.4Al/TNT surface had a porous structure, which would be beneficial for enhancing light absorption and charge transfer. Ti, O, C, N, and Al elements were all well distributed on the surface of the 0.7PCN/0.4Al/TNTs based on elemental mapping (Figure 1F–J). The TEM image further confirmed that the  $\text{g-C}_3\text{N}_4$  modified on 0.7PCN/0.4Al/TNTs exhibited a porous structure (Figure 1K). The lattice spacing of 0.35 nm on the high-resolution transmission electron microscopy (HRTEM) image (Figure 1L) corresponded to the (101) plane of anatase  $\text{TiO}_2$ .<sup>34</sup>

XRD patterns (Figures 2A and S1) were investigated to study the phase composition and structure of the prepared samples. The peaks at around  $25.3^\circ$ ,  $48.0^\circ$ ,  $62.7^\circ$ , and  $75.0^\circ$

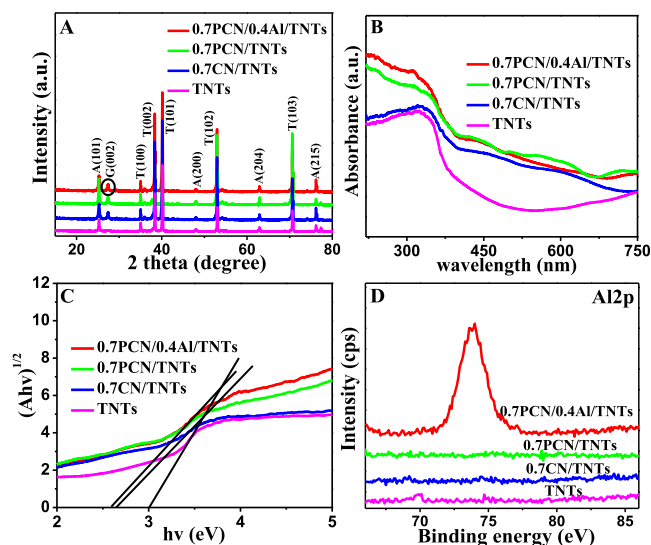


**Figure 2.** (A) XRD patterns (A represents anatase phase from TNTs, T represents the Ti-metal phase from Ti substrate, and G represents  $\text{g-C}_3\text{N}_4$ ). (B) UV-vis absorption reflectance spectra. (C) Tauc plots of transformed Kubelka–Munk function  $[F(R) \cdot hv]^{1/2}$  vs  $h\nu$  (D) Al 2p spectra of different samples.



were attributed to the anatase phase of  $\text{TiO}_2$  derived from TNTs, corresponding to the crystal planes of (101), (200), (204), and (215). The peaks at around  $34.8^\circ$ ,  $38.3^\circ$ ,  $40.2^\circ$ ,  $53.0^\circ$ , and  $70.6^\circ$  were attributed to the Ti-metal phase derived from the Ti substrate, corresponding to the crystal planes of (100), (002), (101), (102), and (103). After modification with CN or PCN, a small characteristic diffraction peak positioned at about  $27.4^\circ$  could be observed, which was attributed to the crystal planes of (002) derived from  $\text{g-C}_3\text{N}_4$ .<sup>35</sup> The phase composition and structure were not influenced by further introduction of Al–O links between TNTs and PCN. The pure TNTs had light absorption in the ultraviolet and visible regions (Figure 2B). The UV light absorption was attributed to its intrinsic band gap and the visible light absorption was attributed to the tubular structure.<sup>34</sup> After PCN modification, an obvious red-shift in the visible light was observed, which was attributed to the adsorption of visible light by the modified PCN and the multiple reflections of incident light within the porous structure of the PCN. To study the variations of the band gaps, the Kubelka–Munk model was used, as described in the following equation

$$(\alpha h\nu)^s = h\nu - E_g \quad (2)$$

where  $\alpha$  is the absorption coefficient,  $h\nu$  is the incident photon energy,  $s = 0.5$  for  $\text{TiO}_2$ , and  $E_g$  is the bandgap. Based on the Kubelka–Munk model, the Tauc plots of the transformed Kubelka–Munk function  $[F(R) \cdot h\nu]^{1/2}$  versus  $h\nu$  (Figures 2C and S2) were examined, where  $F(R) = (1 - R)^2/(2R)$ , and  $R$  is the percentage of the reflected light by the material.<sup>36</sup> Through extending a line from the maximum slope of the curve to the X-axis, it can be obtained that band gaps were 2.56 eV for PCN, 3.01 eV for TNTs, 2.64 eV for 0.7CN/TNTs, and 2.58 eV for 0.7PCN/TNTs. The decreased band gap of 0.7PCN/TNTs that greatly enhanced the visible light absorption of the fabricated composite makes the prepared sample a promising candidate for visible light-driven photocatalytic reactions. After constructing Al–O links in the interfacial connection of PCN and TNTs, there was no obvious change of the band gap for the 0.7PCN/0.4Al/TNTs compared with 0.7PCN/TNTs. The conduction band and valence band potentials of PCN and TNTs were further calculated for confirming the Z-scheme mechanism of the photogenerated charge carriers transfer on the prepared composite with the following formulas<sup>29</sup>

$$E_{\text{VB}} = X - E^e + 0.5E_g \quad (3)$$

$$E_{\text{CB}} = E_{\text{VB}} - E_g \quad (4)$$

where  $E_{\text{VB}}$  indicates the potential of valence band edge,  $X$  indicates the electronegativity of semiconductor,  $E^e$  indicates the energy of free electrons versus hydrogen (about 4.5 eV/NHE), and  $E_{\text{CB}}$  indicates the potential of the conduction band edge. The  $X$  values of  $\text{g-C}_3\text{N}_4$  and  $\text{TiO}_2$  are 4.64 and 5.81 eV.<sup>29,37</sup> From these calculations, the  $E_{\text{VB}}$  and  $E_{\text{CB}}$  of PCN were 1.42 and  $-1.14$  eV/NHE, and the  $E_{\text{VB}}$  and  $E_{\text{CB}}$  of TNTs were 2.81 and  $-0.20$  eV/NHE, respectively.

The surface element composition and chemical states of different samples were investigated by XPS measurements (Figures 2D and S3). The two peaks of  $\text{Ti } 2p_{1/2}$  and  $\text{Ti } 2p_{3/2}$  at the binding energies of 464.1 and 458.3 eV were from  $\text{Ti}^{4+}$  in the  $\text{Ti } 2p$  spectra. The peaks positioned at 531.6 and 529.5 eV in the  $\text{O } 1s$  XPS spectra were derived from the hydroxyl oxygen on the surface of  $\text{TiO}_2$  and the crystal lattice oxygen in

$\text{TiO}_2$ .<sup>38</sup> It can be seen that the hydroxyl oxygen intensity of 0.7PCN/0.4Al/TNTs was higher than that of the TNTs, 0.7CN/TNTs, and 0.7PCN/TNTs because the Al–O links were built between PCN and TNTs through the reaction of dehydration synthesis of  $-\text{Al}-\text{OH}$  groups and the surface adsorbed hydroxyls on the semiconductors with heat treatment. The peaks located at 288.3 and 284.6 eV in the  $\text{C } 1s$  spectra were attributed to the C–N–C band derived from PCN and C–C band derived from adventitious carbon, respectively.<sup>39</sup> The broad peak centered at 399.0 eV in the  $\text{N } 1s$  spectra was derived from the  $\text{sp}^2$ -hybridized nitrogen (C=N–C).<sup>25</sup> Comparing the  $\text{N } 1s$  and  $\text{C } 1s$  (C–N–C) peaks of the three different samples, the binding energies of  $\text{N } 1s$  and  $\text{C } 1s$  (C–N–C) of 0.7PCN/0.4Al/TNTs were lower, which resulted from the electron delocalization effect of the Al–O links. The XPS peak for  $\text{Al } 2p$  of 0.7PCN/0.4Al/TNTs was centered at 73.8 eV.<sup>25</sup> These data together showed that the heterojunction between TNTs and PCN was formed and the Al–O links were successfully introduced into the PCN/TNT heterojunction composites, which would enhance charge transfer.

**Photoelectrochemical Performance.** The photocurrent densities (Figures 3A and S4) of TNTs were enhanced after PCN modification, with the 0.7PCN/TNTs showing the highest photocurrent density among all PCN-modified TNT samples. The 0.7PCN/TNTs showed a higher photocurrent than the 0.7CN/TNTs. After fabrication of Al–O links between PCN and TNTs heterojunctions, photocurrent

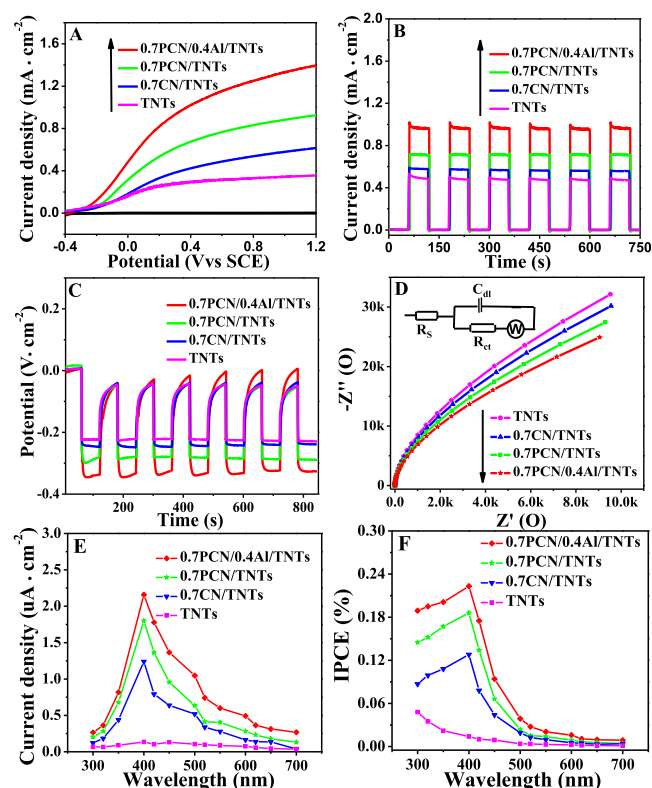


**Figure 3.** (A)  $I$ – $V$  curves (the black lines were measured in dark and colored lines were measured with light irradiation); (B) transient photocurrent response; (C) open circuit potential; (D) equivalent circuit of Nyquist plots for electrochemical impedance spectra; (E) photocurrent densities under different single wavelength; and (F) IPCE of different samples.

densities were further increased. Current densities of all samples with no light irradiation were negligible. The transient photocurrents of all samples were reproducible and thus stable over several on–off cycles with light irradiation (Figures 3B and S5). The fast response of current to light irradiation indicated a quick charge transfer of the TNTs and the modified TNTs. The 0.7PCN/0.4Al/TNTs showed a transient photocurrent density of  $1.02 \text{ mA cm}^{-2}$ , which was 1.9 times that of the pure TNTs ( $0.53 \text{ mA cm}^{-2}$ ), indicating that the PCN and Al–O links greatly improved charge separation. The open-circuit potentials (Figure 3C) were  $-0.34 \text{ V cm}^{-2}$  (7PCN/0.4Al/TNTs),  $-0.28 \text{ V cm}^{-2}$  (0.7PCN/TNT),  $-0.24 \text{ V cm}^{-2}$  (0.7CN/TNTs), and  $-0.22 \text{ V cm}^{-2}$  (TNTs) under light irradiation, demonstrating that 0.7PCN/0.4Al/TNTs had improved photogenerated charge separation, consistent with the photocurrent results.

The data of the electrochemical impedance spectra fitted by the equivalent circuit model of  $R_s(C_{dl}(R_{ct}W))$  were given out (Figure 3D). The 0.7PCN/0.4Al/TNTs sample showed a charge-transfer resistance of  $2.72 \times 10^4 \Omega$ , which was lower than the charge-transfer resistance of TNTs ( $4.12 \times 10^4 \Omega$ ) (Table S1). The decreased charge-transfer resistance demonstrated that the PCN and Al–O links modification facilitated the charge separation and transferability. Based on calculating with single wavelength photocurrent densities (Figure 3E), the IPCE of TNTs was increased by comodification with PCN and Al–O links and 0.7PCN/0.4Al/TNTs, with it having the highest IPCE of 0.223% at 400 nm (Figure 3F), which was 15.9 times of that for the pure TNTs at 400 nm. The enhanced IPCE also indicated an improved photogenerated charge separation of the 0.7PCN/0.4Al/TNTs. Indeed, the IPCE of 0.7PCN/0.4Al/TNTs was not very high. The low IPCE of 0.7PCN/0.4Al/TNTs used in this study indicated a potential for further material improvement. In our future work, we will aim at improving the IPCE of the semiconductor materials.

**Photocatalytic Activity.** The main products of photocatalytic  $\text{CO}_2$  conversion using the pure TNTs were acetic acid ( $14.3 \pm 0.93 \text{ mg L}^{-1} \text{ h}^{-1}$ ), methanol ( $10.8 \pm 1.66 \text{ mg L}^{-1} \text{ h}^{-1}$ ), and formic acid ( $9.9 \pm 1.49 \text{ mg L}^{-1} \text{ h}^{-1}$ ). For PCN-modified TNT composites, the yields of the products varied along with the change of the used mass of the PCN precursor (Figure 4A). When the used mass of the precursor was 0.7 g, the sample showed the highest photocatalytic activity with the concentration of  $35.3 \pm 0.71 \text{ mg L}^{-1} \text{ h}^{-1}$  (acetic acid),  $27.2 \pm 0.58 \text{ mg L}^{-1} \text{ h}^{-1}$  (formic acid), and  $29.8 \pm 0.78 \text{ mg L}^{-1} \text{ h}^{-1}$  for methanol. The production of acetic acid, formic acid, and methanol produced by 0.7PCN/TNTs was higher than that of 0.7CN/TNTs. After fabricating Al–O links between PCN and TNTs heterojunctions using 0.4 M  $\text{AlCl}_3$ , the 0.7PCN/0.4Al/TNTs had improved production of produced chemicals compared with bare TNTs, with increased concentrations by factors of 3.8 for acetic acid ( $54.9 \pm 0.70 \text{ mg L}^{-1} \text{ h}^{-1}$ ), 4.3 for formic acid ( $42.7 \pm 0.54 \text{ mg L}^{-1} \text{ h}^{-1}$ ), and 4.2 for methanol ( $45.4 \pm 0.55 \text{ mg L}^{-1} \text{ h}^{-1}$ ) (Figure 4B). The photocatalytic activities for 2,4-DCP decomposition of TNTs were also improved (Figure 4C,D) with a 40% enhanced decomposition percentage obtained for the 0.7PCN/0.4Al/TNTs. The enhanced activities were due to the elevated optical absorption and charge separation by the PCN and the Al–O links between PCN and TNTs promoting the charge transfer and separation. The prepared sample also showed good stability (Figure S6), with the photocatalytic activity of 0.7PCN/0.4Al/TNTs essentially unchanged over 7 cycles.

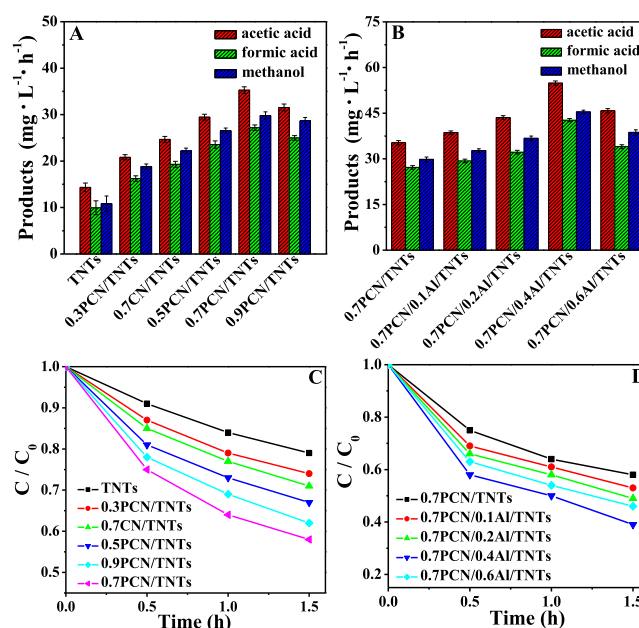


**Figure 4.** Photocatalytic  $\text{CO}_2$  conversion on (A) pure TNTs, g- $\text{C}_3\text{N}_4$ -modified, and PCN-modified TNT composites. (B) PCN/TNT composites and Al–O-linked PCN/TNT composites. Photocatalytic 2,4-DCP decomposition on (C) pure TNTs, g- $\text{C}_3\text{N}_4$ -modified, and PCN-modified TNT composites. (D) Al–O-linked PCN/TNT composites.

**Mechanism Analysis.** To further investigate the charge separation, SPS was used to show that PCN modification enhanced the SPS response, with the 0.7PCN/TNTs having the largest increase compared to the other PCN-modified TNTs (Figures 5A and S7). In addition, 0.7PCN/TNTs showed a higher SPS response than 0.7CN/TNTs, which was due to the porous structure of PCN enhancing visible light absorption and facilitating charge separation. Adding Al–O links between the PCN and TNTs heterojunctions resulted in the largest SPS response for the 0.7PCN/0.4Al/TNTs due to

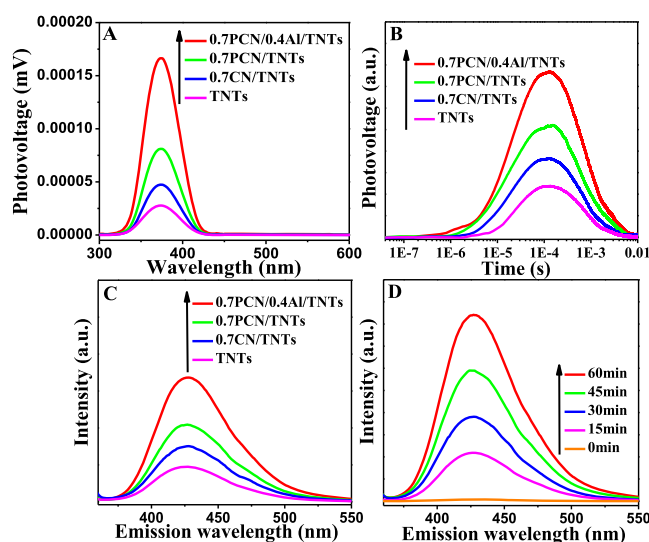


**Figure 5.** (A) SPS responses, (B) TS-SPV responses, and (C) fluorescence spectra of different samples in 1 h light irradiation. (D) Fluorescence spectra changed with light irradiation time on 0.7PCN/0.4Al/TNTs.

facilitation of charge transfer. TS-SPV (Figure 5B) indicated further that the 0.7PCN/0.4Al/TNTs had the highest signal, corresponding to a higher charge separation.

The production of  $\bullet\text{OH}$  radicals, which are the main component of the reactive species produced, reflects the extent of charge separation in the photocatalytic reactions. Their concentrations were also measured using the fluorescence product of 2-hydroxyterephthalic acid, resulting from the reaction of  $\bullet\text{OH}$  with terephthalic acid (Figures 5C and S8). The stronger fluorescence intensity usually corresponds to the higher  $\bullet\text{OH}$  radicals concentration. The fluorescence intensity of TNTs changed with the amount of PCN precursor used, over a range of 0.3–0.9 g, with the highest fluorescence intensity obtained using 0.7 g. With Al–O links added, the highest fluorescence intensity was obtained for the 0.7PCN/0.4Al/TNTs. This increased fluorescence intensity corresponds to the highest concentration of generated  $\bullet\text{OH}$  radicals, and the highest charge separation among all samples. The fluorescence spectra changed with light irradiation time on 0.7PCN/0.4Al/TNTs, demonstrating that the amount of produced  $\bullet\text{OH}$  radicals increased with the prolonged light irradiation time (Figure 5D).

Based on the above results, it can be concluded that the charge transfer on 0.7PCN/0.4Al/TNTs sample complied with the Z-scheme mechanism rather than the traditional heterojunction-type mechanism due to the higher fluorescence intensity of 0.7PCN/TNTs than TNTs. For TNTs, the potential of the valence band edge (2.81 eV) is more positive than the oxidation potentials of  $\text{OH}^-/\bullet\text{OH}$  (1.99 eV) and  $\text{H}_2\text{O}/\bullet\text{OH}$  (2.34 eV); thus, the photogenerated holes of TNTs can react with  $\text{OH}^-$  or  $\text{H}_2\text{O}$  to generate  $\bullet\text{OH}$ . For 0.7PCN/0.4Al/TNTs, if the charge transfer complied with the heterojunction-type mechanism, the photogenerated electrons accumulated on the conduction band of TNTs (−0.20 eV) could not react with  $\text{O}_2$  to generate  $\bullet\text{O}_2^-$  ( $\text{O}_2/\text{O}_2^-$  −0.33 eV) and further lead to the generation of  $\bullet\text{OH}$ , the photogenerated holes accumulated on the valence band of PCN (1.42 eV) could not react with  $\text{OH}^-$  or  $\text{H}_2\text{O}$  to form  $\bullet\text{OH}$ , and hence, the 0.7PCN/0.4Al/TNTs sample would show no fluorescence intensity. However, the fluorescence intensity of 0.7PCN/0.4Al/TNTs detected was much higher than that of TNTs. Thus, it can be concluded that the charge transfer on 0.7PCN/0.4Al/TNTs was consistent with the Z-scheme mechanism, and the photogenerated electrons of TNTs transferred from the conduction band of TNTs to the valence band of PCN via Al–O links and recombined with the photogenerated holes of PCN. The photogenerated electrons on the conduction band of PCN (−1.14 eV) could reduce the dissolved  $\text{O}_2$  into  $\bullet\text{O}_2^-$  and further lead to the generation of  $\bullet\text{OH}$ , the photogenerated holes on the valence band of TNTs could react with  $\text{OH}^-$  or  $\text{H}_2\text{O}$  to form  $\bullet\text{OH}$ , leading to an enhanced fluorescence intensity.

The overall scheme by which the photogenerated charge transfer and separation was enhanced for the fabricated Al–O-linked PCN/TNT composites is summarized in Figure 6. When both TNTs and PCN were excited concurrently, the photogenerated electrons of TNTs recombined with the photogenerated holes of PCN, leaving the separated holes of TNTs and electrons of PCN with enough energy to take part in the related redox reactions. Thus, the charge separation and photocatalytic activities would be elevated. With the added Al–O links between TNTs and PCN, the charge transfer from TNTs to PCN was increased and thus it benefited charge

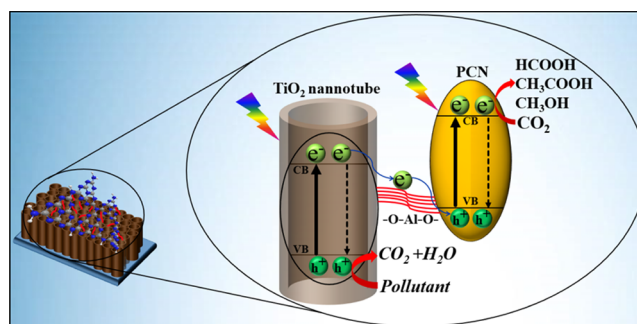


**Figure 6.** Schematic of the charge transfer and separation for the built Al–O-linked PCN/TNT composites.

separation, further promoting the photocatalytic  $\text{CO}_2$  conversion or 2,4-DCP decomposition.

## CONCLUSIONS

We successfully built the Z-scheme heterojunctional composites of TNTs with PCN and created Al–O links between TNTs and PCN. The obtained Al–O-linked PCN/TNT composites exhibited an enhanced photocatalytic performance for  $\text{CO}_2$  conversion to organic acids or methanol and 2,4-DCP decomposition. These improvements were due to the porous framework of the g- $\text{C}_3\text{N}_4$  enhancing the absorption of visible light and charge separation and the effective Al–O links facilitating charge transfer. This work offers us a feasible approach to design efficient Al–O-linked Z-scheme composites for efficient energy production and pollutant degradation and helps us to further understand charge separation and transfer mechanism in Z-scheme composites.

## ASSOCIATED CONTENT

### Supporting Information

The Supporting Information is available free of charge on the ACS Publications website at DOI: 10.1021/acssuschemeng.9b02489.

XRD patterns, UV–vis absorption reflectance spectra, XPS spectra,  $I$ – $V$  curves, transient photocurrent response, EIS parameters, photocatalytic stability tests, SPS responses, and fluorescence spectra (PDF)

## AUTHOR INFORMATION

### Corresponding Authors

\*E-mail: lidacumt@163.com. Phone: (+86) 451-86287017. Fax: (+86) 451-86287017 (D.L.).  
\*E-mail: jia14921@163.com (J.L.).

### ORCID

Yujie Feng: 0000-0001-8342-5482

Jia Liu: 0000-0001-8334-9547

### Notes

The authors declare no competing financial interest.

## ACKNOWLEDGMENTS

This work was supported by the National Key R&D Program of China (grant no. 2016YFE0106500), National Natural Science Fund of China (grant nos. 21673061 and 51408156), and the National Key R&D Program of China (grant no. 2016YFC0401101). The authors also acknowledge the project funded by China Postdoctoral Science Foundation (grant no. 2017M621265) and the Open Project of State Key Laboratory



of Urban Water Resource and Environment, Harbin Institute of Technology (no. QA201935).

## REFERENCES

- (1) Wei, Y.; Wu, X.; Zhao, Y.; Wang, L.; Zhao, Z.; Huang, X.; Liu, J.; Li, J. Efficient photocatalysts of TiO<sub>2</sub> nanocrystals-supported Pt-Ru alloy nanoparticles for CO<sub>2</sub> reduction with H<sub>2</sub>O: synergistic effect of Pt-Ru. *Appl. Catal., B* **2018**, *236*, 445–457.
- (2) Jiao, J.; Wei, Y.; Zhao, Y.; Zhao, Z.; Duan, A.; Liu, J.; Pang, Y.; Li, J.; Jiang, G.; Wang, Y. AuPd/3DOM-TiO<sub>2</sub> catalysts for photocatalytic reduction of CO<sub>2</sub>: High efficient separation of photogenerated charge carriers. *Appl. Catal., B* **2017**, *209*, 228–239.
- (3) Zhao, Y.; Wei, Y.; Wu, X.; Zheng, H.; Zhao, Z.; Liu, J.; Li, J. Graphene-wrapped Pt/TiO<sub>2</sub> photocatalysts with enhanced photo-generated charges separation and reactant adsorption for high selective photoreduction of CO<sub>2</sub> to CH<sub>4</sub>. *Appl. Catal., B* **2018**, *226*, 360–372.
- (4) Wang, M.; Iocozia, J.; Sun, L.; Lin, C.; Lin, Z. Inorganic-modified semiconductor TiO<sub>2</sub> nanotube arrays for photocatalysis. *Energy Environ. Sci.* **2014**, *7*, 2182–2202.
- (5) Liang, H.; Meng, Q.; Wang, X.; Zhang, H.; Wang, J. Nanoplasmonically engineered interfaces on amorphous TiO<sub>2</sub> for highly efficient photocatalysis in hydrogen evolution. *ACS Appl. Mater. Interfaces* **2018**, *10*, 14145–14152.
- (6) Chen, B.; Meng, Y.; Sha, J.; Zhong, C.; Hu, W.; Zhao, N. Preparation of MoS<sub>2</sub>/TiO<sub>2</sub> based nanocomposites for photocatalysis and rechargeable batteries: progress, challenges, and perspective. *Nanoscale* **2017**, *10*, 34–68.
- (7) Wu, L.; Li, F.; Xu, Y.; Zhang, J. W.; Zhang, D.; Li, G.; Li, H. Plasmon-induced photoelectrocatalytic activity of Au nanoparticles enhanced TiO<sub>2</sub> nanotube arrays electrodes for environmental remediation. *Appl. Catal., B* **2015**, *164*, 217–224.
- (8) Ye, M.; Gong, J.; Lai, Y.; Lin, C.; Lin, Z. High-efficiency photoelectrocatalytic hydrogen generation enabled by palladium quantum dots-sensitized TiO<sub>2</sub> nanotube arrays. *J. Am. Chem. Soc.* **2012**, *134*, 15720–15723.
- (9) Sun, Q.; Peng, Y.-P.; Chen, H.; Chang, K.-L.; Qiu, Y.-N.; Lai, S.-W. Photoelectrochemical oxidation of ibuprofen via Cu<sub>2</sub>O-doped TiO<sub>2</sub> nanotube arrays. *J. Hazard. Mater.* **2016**, *319*, 121–129.
- (10) Szkoda, M.; Siuzdak, K.; Lisowska-Oleksiak, A.; Karczewski, J.; Ryl, J. Facile preparation of extremely photoactive boron-doped TiO<sub>2</sub> nanotubes arrays. *Electrochem. Commun.* **2015**, *60*, 212–215.
- (11) Loeb, S. K.; Alvarez, P. J. J.; Brame, J. A.; Cates, E. L.; Choi, W.; Crittenden, J.; Dionysiou, D. D.; Li, Q.; Li-Puma, G.; Quan, X.; Sedlak, D. L.; David Waite, T.; Westerhoff, P.; Kim, J.-H. The technology horizon for photocatalytic water treatment: sunrise or sunset? *Environ. Sci. Technol.* **2019**, *53*, 2937–2947.
- (12) Wang, H.; Liang, Y.; Liu, L.; Hu, J.; Cui, W. Highly ordered TiO<sub>2</sub> nanotube arrays wrapped with g-C<sub>3</sub>N<sub>4</sub> nanoparticles for efficient charge separation and increased photoelectrocatalytic degradation of phenol. *J. Hazard. Mater.* **2018**, *344*, 369–380.
- (13) Wang, B.; Cao, J.-T.; Dong, Y.-X.; Liu, F.-R.; Fu, X.-L.; Ren, S.-W.; Ma, S.-H.; Liu, Y.-M. An in situ electron donor consumption strategy for photoelectrochemical biosensing of proteins based on ternary Bi<sub>2</sub>S<sub>3</sub>/Ag<sub>2</sub>S/TiO<sub>2</sub> NT arrays. *Chem. Commun.* **2018**, *54*, 806–809.
- (14) Zhou, Q.; Xing, A.; Li, J.; Zhao, D.; Zhao, K.; Lei, M. Synergistic enhancement in photoelectrocatalytic degradation of bisphenol A by CeO<sub>2</sub> and reduced graphene oxide co-modified TiO<sub>2</sub> nanotube arrays in combination with Fenton oxidation. *Electrochim. Acta* **2016**, *209*, 379–388.
- (15) Hu, L.; Fong, C.-C.; Zhang, X.; Chan, L. L.; Lam, P. K. S.; Chu, P. K.; Wong, K.-Y.; Yang, M. Au nanoparticles decorated TiO<sub>2</sub> nanotube arrays as a recyclable sensor for photoenhanced electrochemical detection of bisphenol A. *Environ. Sci. Technol.* **2016**, *50*, 4430–4438.
- (16) Yoo, J.; Altomare, M.; Mokhtar, M.; Alshehri, A.; Al-Thabaiti, S. A.; Mazare, A.; Schmuki, P. Photocatalytic H<sub>2</sub> generation using dewetted Pt-decorated TiO<sub>2</sub> nanotubes: optimized dewetting and oxide crystallization by a multiple annealing process. *J. Phys. Chem. C* **2016**, *120*, 15884–15892.
- (17) Zhang, Q.; Ye, S.; Chen, X.; Song, X.; Li, L.; Huang, X. Photocatalytic degradation of ethylene using titanium dioxide nanotube arrays with Ag and reduced graphene oxide irradiated by γ-ray radiolysis. *Appl. Catal., B* **2017**, *203*, 673–683.
- (18) Li, H.; Xia, Z.; Chen, J.; Lei, L.; Xing, J. Constructing ternary CdS/reduced graphene oxide/TiO<sub>2</sub> nanotube arrays hybrids for enhanced visible-light-driven photoelectrochemical and photocatalytic activity. *Appl. Catal., B* **2015**, *168–169*, 105–113.
- (19) Barr, M. K. S.; Assaud, L.; Brazeau, N.; Hanbücken, M.; Ntais, S.; Santinacci, L.; Baranova, E. A. Enhancement of Pd catalytic activity toward ethanol electrooxidation by atomic layer deposition of SnO<sub>2</sub> onto TiO<sub>2</sub> nanotubes. *J. Phys. Chem. C* **2017**, *121*, 17727–17736.
- (20) Jang, J. S.; Ahn, C. W.; Won, S. S.; Kim, J. H.; Choi, W.; Lee, B.-S.; Yoon, J.-H.; Kim, H. G.; Lee, J. S. Vertically aligned core-shell PbTiO<sub>3</sub>@TiO<sub>2</sub> heterojunction nanotube array for photoelectrochemical and photocatalytic applications. *J. Phys. Chem. C* **2017**, *121*, 15063–15070.
- (21) Yu, X.; Wang, L.; Zhang, J.; Guo, W.; Zhao, Z.; Qin, Y.; Mou, X.; Li, A.; Liu, H. Hierarchical hybrid nanostructures of Sn<sub>3</sub>O<sub>4</sub> on N doped TiO<sub>2</sub> nanotubes with enhanced photocatalytic performance. *J. Mater. Chem. A* **2015**, *3*, 19129–19136.
- (22) Li, K.; Huang, Z.; Zeng, X.; Huang, B.; Gao, S.; Lu, J. Synergetic effect of Ti<sup>(3+)</sup> and oxygen doping on enhancing photoelectrochemical and photocatalytic properties of TiO<sub>2</sub>/g-C<sub>3</sub>N<sub>4</sub> heterojunctions. *ACS Appl. Mater. Interfaces* **2017**, *9*, 11577–11586.
- (23) Wei, H.; McMaster, W. A.; Tan, J. Z. Y.; Cao, L.; Chen, D.; Caruso, R. A. Mesoporous TiO<sub>2</sub>/g-C<sub>3</sub>N<sub>4</sub> microspheres with enhanced visible-light photocatalytic activity. *J. Phys. Chem. C* **2017**, *121*, 22114–22122.
- (24) Liao, W.; Murugananthan, M.; Zhang, Y. Synthesis of Z-scheme g-C<sub>3</sub>N<sub>4</sub>-Ti<sup>(3+)</sup>/TiO<sub>2</sub> material: an efficient visible light photoelectrocatalyst for degradation of phenol. *Phys. Chem. Chem. Phys.* **2015**, *17*, 8877–8884.
- (25) Wang, J.; Qin, C.; Wang, H.; Chu, M.; Zada, A.; Zhang, X.; Li, J.; Raziq, F.; Qu, Y.; Jing, L. Exceptional photocatalytic activities for CO<sub>2</sub> conversion on Al-O bridged g-C<sub>3</sub>N<sub>4</sub>/α-Fe<sub>2</sub>O<sub>3</sub> z-scheme nanocomposites and mechanism insight with isotopes. *Appl. Catal., B* **2018**, *221*, 459–466.
- (26) Zhou, D.; Chen, Z.; Yang, Q.; Shen, C.; Tang, G.; Zhao, S.; Zhang, J.; Chen, D.; Wei, Q.; Dong, X. Facile construction of g-C<sub>3</sub>N<sub>4</sub> nanosheets/TiO<sub>2</sub> nanotube arrays as Z-scheme photocatalyst with enhanced visible-light performance. *ChemCatChem* **2016**, *8*, 3064–3073.
- (27) Fu, J.; Zhu, B.; Jiang, C.; Cheng, B.; You, W.; Yu, J. Hierarchical porous O-doped g-C<sub>3</sub>N<sub>4</sub> with enhanced photocatalytic CO<sub>2</sub> reduction activity. *Small* **2017**, *13*, 1603938–1603947.
- (28) Chen, Z.; Lu, S.; Wu, Q.; He, F.; Zhao, N.; He, C.; Shi, C. Salt-assisted synthesis of 3D open porous g-C<sub>3</sub>N<sub>4</sub> decorated with cyano groups for photocatalytic hydrogen evolution. *Nanoscale* **2018**, *10*, 3008–3013.
- (29) Chen, X.; Li, H.; Wu, Y.; Wu, H.; Wu, L.; Tan, P.; Pan, J.; Xiong, X. Facile fabrication of novel porous graphitic carbon nitride/copper sulfide nanocomposites with enhanced visible light driven photocatalytic performance. *J. Colloid Interface Sci.* **2016**, *476*, 132–143.
- (30) Xiao, J.; Xie, Y.; Nawaz, F.; Wang, Y.; Du, P.; Cao, H. Dramatic coupling of visible light with ozone on honeycomb-like porous g-C<sub>3</sub>N<sub>4</sub> towards superior oxidation of water pollutants. *Appl. Catal., B* **2016**, *183*, 417–425.
- (31) Luan, P.; Xie, M.; Fu, X.; Qu, Y.; Sun, X.; Jing, L. Improved photoactivity of TiO<sub>2</sub>-Fe<sub>2</sub>O<sub>3</sub> nanocomposites for visible-light water splitting after phosphate bridging and its mechanism. *Phys. Chem. Chem. Phys.* **2015**, *17*, 5043–5050.
- (32) Fu, X.; Xie, M.; Luan, P.; Jing, L. Effective visible-excited charge separation in silicate-bridged ZnO/BiVO<sub>4</sub> nanocomposite and its contribution to enhanced photocatalytic activity. *ACS Appl. Mater. Interfaces* **2014**, *6*, 18550–18557.

- (33) Ates, M.; Bayrak, Y.; Yoruk, O.; Caliskan, S. Reduced graphene oxide/titanium oxide nanocomposite synthesis via microwave-assisted method and supercapacitor behaviors. *J. Alloys Compd.* **2017**, *728*, 541–551.
- (34) Wu, J.; Li, D.; Liu, J.; Li, C.; Li, Z.; Logan, B. E.; Feng, Y. Enhanced charge separation of TiO<sub>2</sub> nanotubes photoelectrode for efficient conversion of CO<sub>2</sub>. *ACS Sustainable Chem. Eng.* **2018**, *6*, 12953–12960.
- (35) Li, J.; Zhang, X.; Raziq, F.; Wang, J.; Liu, C.; Liu, Y.; Sun, J.; Yan, R.; Qu, B.; Qin, C.; Jing, L. Improved photocatalytic activities of g-C<sub>3</sub>N<sub>4</sub> nanosheets by effectively trapping holes with halogen-induced surface polarization and 2,4-dichlorophenol decomposition mechanism. *Appl. Catal., B* **2017**, *218*, 60–67.
- (36) Bjelajac, A.; Djokic, V.; Petrovic, R.; Socol, G.; Mihailescu, I. N.; Florea, I.; Ersen, O.; Janackovic, D. Visible light-harvesting of TiO<sub>2</sub> nanotubes array by pulsed laser deposited CdS. *Appl. Surf. Sci.* **2014**, *309*, 225–230.
- (37) Cao, H.; Lu, Y.; Ning, W.; Zhang, H.; Zheng, G. Co<sub>3</sub>O<sub>4</sub> nanoparticles modified TiO<sub>2</sub> nanotube arrays with improved photoelectrochemical performance. *Russ. J. Appl. Chem.* **2019**, *92*, 64–70.
- (38) Wu, J.; Cui, H.; Zhang, X.; Luan, Y.; Jing, L. Enhanced photocatalytic activity of Cl-residual rutile TiO<sub>2</sub> nanorods after targeted co-modification with phosphoric and boric acids. *Phys. Chem. Chem. Phys.* **2015**, *17*, 15837–15842.
- (39) Liu, L.; Zhang, G.; Irvine, J. T. S.; Wu, Y. Organic semiconductor g-C<sub>3</sub>N<sub>4</sub> modified TiO<sub>2</sub> nanotube arrays for enhanced photoelectrochemical performance in wastewater treatment. *Energy Technol.* **2015**, *3*, 982–988.